

# Feedback Motion Planning for Liquid Transfer using Supervised Learning

Zherong Pan<sup>1</sup> and Dinesh Manocha<sup>1</sup>

**Abstract**—We present a novel motion planning algorithm for transferring a liquid body from a source to a target container. Our approach uses a receding-horizon optimization strategy that takes into account fluid constraints and avoids collisions. In order to efficiently handle the high-dimensional configuration space of a liquid body, we use system identification to learn its dynamics characteristics using a neural network. We generate the training dataset using stochastic optimization in a transfer-problem-specific search space. The runtime feedback motion planner is used for real-time planning and we observe high success rate in our simulated 2D and 3D fluid transfer benchmarks.

## I. INTRODUCTION

Robotic manipulation of non-rigid objects such as fluids, elastic bodies, and strings is a challenging problem that arises in different applications. In this paper, we address the problem of fluid manipulation, where the goal is to use a robot to transfer a liquid body from a source container to a target container. Such liquid transfer tasks arise as industrial robots are used for painting, cleaning, or dispensing lubricants. Other applications include use of service robots for cooking, cleaning, or feeding.

A key issue for motion planning algorithms is to satisfy the fluid dynamics constraints. The fluid body can have a complex topology and undergo large deformations. The underlying solvers tend to use a large number of particles (tens of thousands) to model their motion. This results in a very high dimensional configuration space of the liquid body and makes it hard to directly use sampling-based motion planning algorithms. Other techniques based on optimization-based planner [1], [2] may not work well because the free-surface of a liquid body introduces non-smooth changes.

Prior planning algorithms for fluid manipulation are either based on demonstration and learning methods, or use dynamics constraints. The demonstration and learning methods need a large number of example trajectories and current methods may not generalize to new scenarios. Some techniques take into account full-featured fluid dynamics model [3], [4], but have a very high computational overhead and are limited to simple scenarios. Some of the commonly used methods are based on reduced or simplified dynamics models [5], [6], [7], where many liquid dynamics constraints are ignored and they are combined with open-loop planners. As a result, any small error in the dynamics formulation can become uncontrollable and grow significantly over longer horizons.

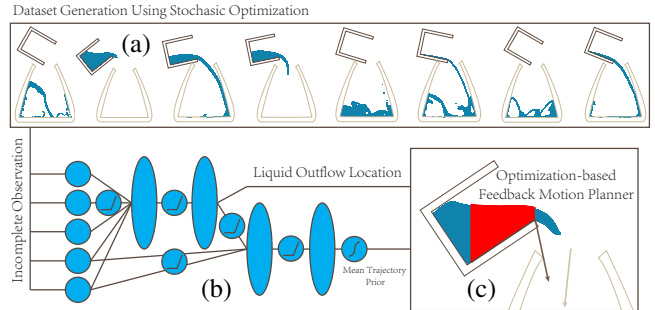


**Fig. 1:** An illustration of our feedback motion planning framework. From the training dataset found by stochastic optimization (a), we train a neural network that predicts both the liquid outflow position and the mean trajectory prior (b). Our online planner tries to determine the source container trajectory from an incomplete observation (c), e.g., the liquid height field in red and the moving speed of the source/target containers (the two arrows).

A common technique to address some of these issues is based on using feedback motion planners. However, such planners need to make decisions rather quickly and therefore, can't rely on using fluid simulators to satisfy the underlying constraints. In practice, accurate fluid simulators can take minutes in a 2D or hours in a 3D workspace. As a result, we need different techniques that can provide a good approximation of the dynamic state of the liquid body, and have a low runtime overhead.

**Main Results:** We present a novel feedback planning algorithm for liquid transfer. As part of the preprocess, we use a system identification technique to predict the dynamic characteristics of a liquid body using supervised learning. The learning algorithm has two main components: training dataset generation and supervised learning. The training dataset is generated offline using a large number of random configurations of liquid transfer problems. These configurations are generated by changing the relative location of two containers, the amount of liquid in the source container, and the speed of the target container movement. Moreover, we compute the optimal liquid transfer trajectory for each configuration using stochastic optimization, which uses a fully-featured liquid simulator. Given these trajectories, we extract a groundtruth incomplete liquid observation (the height field of free-surface) from each training sample to generate our dataset and use that to train a four layer neural network. During online feedback motion planning, we take into account the height field of free-surface and the location of two containers using the trained neural network. Our planner then determines the desired speed of the source container from a spacetime optimization over a short horizon

<sup>1</sup> Department of Computer Science, the University of North Carolina at Chapel Hill {zherong, dm}@cs.unc.edu

and also takes into account collision avoidance constraints.

We have evaluated our algorithm on many new and challenging scenarios that are quite different from training dataset configurations. In practice, our learning-based planner achieves almost the same success rate as the groundtruth trajectory in our training dataset. Moreover, we have also tested our planner in 3D workspaces and on fluids with different physical characteristics (e.g. viscosity). Our results show that, although our training dataset uses a single low-viscous fluid material, the trained neural network can be used for pouring fluids with much larger viscosity.

The rest of the paper is organized as follows: We briefly survey prior works in motion planning and fluid simulation in Section II; We introduce our notation and give an overview of the approach in Section III; In Section III-A and Section IV, we present the feedback motion planning algorithm and the process for learning dynamic characteristics, respectively. We highlight its performance and effectiveness on 2D and 3D benchmarks in Section V.

## II. RELATED WORKS

Our approach builds on three areas of prior work: motion planning, planning for dynamics objects, and reinforcement learning.

### A. GENERAL MOTION PLANNING

A motion planning algorithm searches for a trajectory that satisfies a set of constraints (collision-free, smoothness), which may also be optimal under a given quality measure. Many early motion planners such as [8] and its descendants [9], [10], [11] consider only collision-free constraints. Unlike these methods that tend to compute a trajectory by sampling in the space of possible trajectories, optimization-based motion planners such as [2], [1], [12] can easily take into account other constraints, such as dynamics, smoothness, etc. Many of these approaches formulate the problem as a spacetime continuous optimization. Such optimization methods have also been used for liquid transfer [4], [7] based on simplified dynamics and limited to static scenarios.

There is considerable work on feedback motion planning that uses refinement schemes based on feedback control laws. This can be performed using replanning [13], [14], [15] or by formulating the problem as a Markov Decision Process [16], [17]. These ideas have been applied to high dimensional continuous systems such as humanoid robots [18], [19]. We present a feedback motion planning algorithm for liquid transfer.

### B. PLANNING FOR DYNAMIC OBJECTS

The extension of conventional motion planning algorithms to the manipulation of non-rigid objects has been addressed in the context of virtual suturing [20], cloth folding [21], and surgical simulation [22]. It can be challenging to deal with non-rigid objects with high-dimensional configuration spaces. This is especially the case with liquid manipulation tasks, where the dimension can be as high as several million (see [4] for a detailed discussion). For certain types of

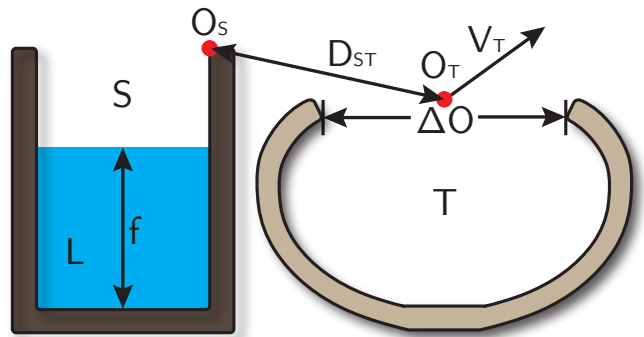


**Fig. 2: Notation** used in the paper: the source container  $S$ , its lip of opening  $O_S$ , the target container  $T$ , its center of opening  $O_T$ , the opening width  $\Delta O$ , the liquid body  $L$ , and fill level  $f$ . We allow variations in the distance  $D_{ST}$  between  $O_S$  and  $O_T$ , as well as the moving speed ( $V_T$ ) of the target container.

fluid such as smoke and fire, optimization-based motion planning can be adapted to solve the problem by exploiting the special structure of the resulting fluid simulator [23], [24]. However, it is non-trivial to extend these methods to control liquid bodies with non-smooth, rapidly-changing free surfaces. Moreover, prior methods are designed for offline applications and computationally very costly. Previous work [7] reduced the cost by using a much simplified liquid model, dependent on just two variables.

### C. IMITATION OR REINFORCEMENT LEARNING

Our approach is based on reinforcement learning [16]. Reinforcement learning techniques have been shown to be effective in terms of controlling high dimensional dynamic systems, e.g., a humanoid robot [18], [25]. Recently, imitation learning has been used to perform liquid manipulation using example container trajectories from a human demonstrator [26]. However, the learning framework in their work does not take fluid dynamics constraints into account. Therefore, prior methods cannot handle fluid-related variations in the environment. In addition, training data acquisition for imitation learning is non-trivial. In order for the learning framework to be aware of fluid dynamics, trajectories of liquid body shapes from real-life experiments have to be captured and digitized, which is challenging in and of itself (see [27], [28]).

## III. PROBLEM STATEMENT

In this section, we first introduce the notation for formulating the liquid pouring problem, denoted by  $P$ , in the continuous case. The configuration for an instance of  $P$  is illustrated in Figure 2, where we have a source container denoted by rigid body  $S$ , a target container denoted by  $T$ , and the liquid body denoted by  $L$ . Without ambiguity, we also use these symbols  $S$ ,  $T$  and  $L$  to denote the closed set occupied by the three bodies. Initially,  $S$  and  $T$  are oriented upright and  $L \subset S$ , as illustrated in Figure 2. Two geometric features in  $S$  and  $T$  play an important role in our method: the lip of source container opening  $O_S$ , and the center and width of target container opening  $O_T$  and  $\Delta O$ , respectively. These points are defined in their local coordinate system,

and the local to global transformation is denoted by  $\mathbf{R}_S(t)$  and  $\mathbf{R}_T(t)$ , where  $t$  is the current time. Finally, we allow the following variations in defining different instances or configurations of the liquid pouring problem:

- The initial relative location  $\mathbf{D}_{ST} \triangleq \mathbf{R}_S(0)\mathbf{O}_S - \mathbf{R}_T(0)\mathbf{O}_T$  is allowed to change in the range  $\mathbf{D}_{ST} \in [-L, 0] \times [-L, L]$ . This means that  $\mathbf{S}$  is always on the left of  $\mathbf{T}$ . The formulation is symmetric otherwise.
- Throughout the motion planning procedure,  $\mathbf{T}$  should always be oriented upright, but is allowed to move with a constant speed  $\mathbf{V}_T \in [-V, V]^2$ . As a result, we have:

$$\mathbf{R}_S(t) = \begin{pmatrix} \cos(\alpha(t)) & -\sin(\alpha(t)) & x_S(t) \\ \sin(\alpha(t)) & \cos(\alpha(t)) & y_S(t) \\ & & 1 \end{pmatrix} \quad \mathbf{R}_T(t) = \begin{pmatrix} 1 & \mathbf{V}_T^x t \\ & 1 & \mathbf{V}_T^y t \\ & & 1 \end{pmatrix},$$

where  $(x_S, y_S, \alpha)(t)$  are the location and turning angle of  $\mathbf{S}$ .

- The amount of liquid in  $\mathbf{S}$  is allowed to change, denoted by fill level  $f$  where  $f \in [f_{min}, f_{max}]$ .

In summary, we can denote one instance of liquid transfer problem by  $\mathbf{P}(\mathbf{D}_{ST}, \mathbf{V}_T, f)$ . The goal of our feedback motion planner is to determine the source container trajectory  $\mathbf{R}_S(t)$ . Given a specific problem  $\mathbf{P}$  and trajectory  $\mathbf{R}_S(t)$ , a corresponding trajectory of liquid body,  $\mathbf{L}(t)$ , can be computed by time integrating the liquid governing equation, the Navier-Stokes equation:

$$\begin{aligned} \frac{Du}{Dt} &= \mu \nabla \cdot (\nabla u + \nabla u^T) + g - \nabla p \quad \nabla \cdot u = 0 \quad (1) \\ \text{s.t.} \quad u(x) &= \dot{\mathbf{R}}_S(t)x \quad x \in \partial \mathbf{S} \cap \partial \mathbf{L} \\ u(x) &= \dot{\mathbf{R}}_T(t)x \quad x \in \partial \mathbf{T} \cap \partial \mathbf{L}, \end{aligned}$$

where  $u, \mu, g, p$  are the liquid velocity field, liquid viscosity coefficient, gravity, and pressure, respectively. The advection term  $\frac{Du}{Dt}$  allows continuous shape deformation, which makes it very challenging to model, perceive, or predict the liquid shape. Therefore, the liquid body shape is also a function of  $\mathbf{R}_S(t)$ , denoted by  $\mathbf{L}[\mathbf{R}_S](t)$ , and we use a shortcut notation  $\mathbf{L}(t)$  to represent it.

In practice, we define a discrete version of the problem using a particle-based spatial discretization scheme, the finite-difference temporal discretization scheme and the same particle-based fluid simulator as [4]. As a result, each of the sets  $\mathbf{S}, \mathbf{T}$  and  $\mathbf{L}(t)$  becomes a set of particles  $\{P_S\}, \{P_T\}$  and  $\{P_L(t)\}$ , respectively, where each particle  $P_{S,T,L}^i$  occupies a circle with a fixed radius as illustrated in Figure 3 (a). Finally, the discrete motion plan  $\mathcal{P}$  is represented by a uniform sampling  $\mathbf{R}_S(t): \mathcal{P} = \{\mathbf{R}_S(t_i) | t_i = i\Delta t, 0 \leq i \leq N\}$ . Here we again use the shortcut notation  $P_L(t)$  instead of  $P_L(t, \mathcal{P})$  without ambiguity.

### A. FEEDBACK MOTION PLANNING

Given a transfer problem  $\mathbf{P}$ , we use a receding horizon feedback motion planner to search for the discrete plan  $\mathcal{P}$ . Specifically, during each time instance  $t_i$ , we solve a spacetime optimization problem:

$$\begin{aligned} \text{argmin}_{\dot{\mathbf{R}}_S(t_i), \dots, \dot{\mathbf{R}}_S(t_{i+K})} \sum_{0 \leq k \leq K} C(t_{i+k}) \quad (2) \\ C(t) \triangleq C_l(t) + C_r(t) + C_o(t), \end{aligned}$$

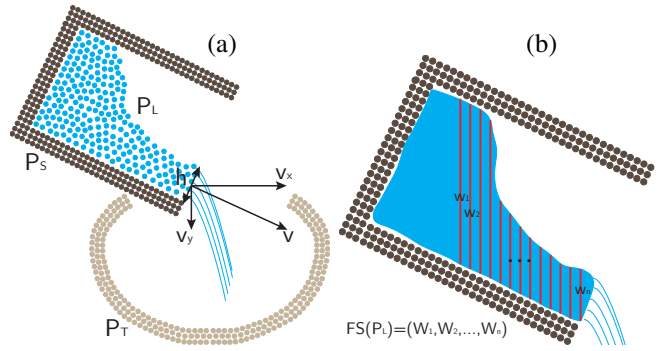


**Fig. 3:** (a): A discrete setting of liquid transfer problem using particle-based spatial discretization scheme: source container particles  $\{P_S\}$  in brown, target container particles  $\{P_T\}$  in gray and liquid particles  $\{P_L(t)\}$  in blue. We assume that each  $P_L^i(t)$  leaving the cup will follow a quadratic curve with outflowing velocity  $(v_x, v_y)$  and outflowing cross-section height  $h$ . (b): The free-surface is sampled to get the liquid height fields,  $FS(P_L) = (W_1, W_2, \dots, W_n)$ , where each  $W_i$  is the vertical distance between free surface of  $\mathbf{L}$  and  $\mathbf{S}$ .

over  $K$  timesteps and then use the control  $\dot{\mathbf{R}}_S(t_i)$ . Here  $\dot{\mathbf{R}}_S = (\dot{x}_S, \dot{y}_S, \dot{\alpha})$ .

Our objective function involves three terms: The first term  $C_l(t)$  requires liquid to fall into  $\mathbf{T}$ ,  $C_r(t)$  is a regularization term, and finally  $C_o(t)$  penalizes any collisions between  $\mathbf{R}_S(t)\mathbf{S}$  and  $\mathbf{R}_T(t)\mathbf{T}$ . We can use the same  $C_o(t)$  as [12], [4] to avoid collision with obstacles in the environment. However, since  $C_r(t)$  brings  $\mathbf{R}_S(t)$  close to a collision-free mean trajectory, we never observe any collision between the two containers, so we focus on only  $C_l(t)$  and  $C_r(t)$ . As illustrated in Figure 3, we assume that the liquid particles leaving  $\mathbf{S}$  at current time instance  $t$  will follow a quadratic curve. This curve can be parameterized using 4 parameters in 2D and 6 parameters in 3D: the outflow velocity  $(v_x, v_y)$ , the outflow cross section height  $h$ , and the outflow flux  $\rho$ . We use the additional parameter  $\rho$  as an indicator of whether or not there is liquid flowing out at  $t$ . The four parameters  $(v_x, v_y, h, \rho)$  determine the liquid outflow position. The term  $C_l(t)$  is used to penalize the closest distance between this quadratic curve and  $\mathbf{R}_T(t)\mathbf{O}_T$ :

$$C_l(t) = \max(\rho, 0) \inf_t \|\text{curve}(v_x, v_y, h, t) - \mathbf{R}_T(t)\mathbf{O}_T\|^2,$$

where the norm in the above equation takes the form of a quartic polynomial so that the infimum can be computed analytically. Finally, the regularization term  $C_r(t)$  penalizes the distance between the optimized trajectory and a so-called mean trajectory prior:

$$C_r(t) = \|\dot{\mathbf{R}}_S(t) - \dot{\mathbf{R}}_S^*(t)\|^2.$$

Given the set of parameters  $(v_x, v_y, h, \rho, \dot{\mathbf{R}}_S^*)(t)$ , we have completed the definition of our objective function for the receding horizon spacetime optimization. We assume that these parameters can be inferred from the observations of the current system configuration: the odometry of source container  $\mathbf{R}_S$ , the odometry of target container  $\mathbf{R}_T$ , and the liquid body  $\mathbf{L}$ . We assume that  $\mathbf{R}_S$  and  $\mathbf{R}_T$  can be fully

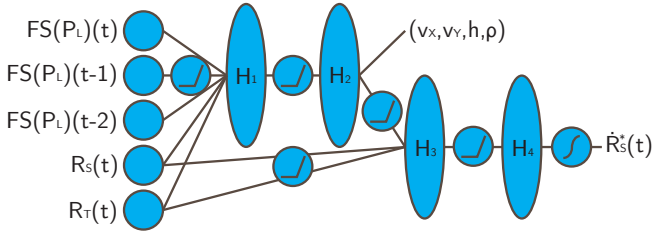


**Fig. 4:** Our 4-layer neural network structure for parameter estimation. We use ReLU activation function for all internal layers and Sigmoid activation function for the output layer.

observed, but we have only partial information of  $\mathbf{L}$ . Specifically, we can only observe the liquid height field  $FS(\mathbf{L})$  as illustrated in Figure 3 (b). Such height field information can be computed by sampling the reconstructed free-surface in a simulated environment. In summary, the parameter inference algorithm needs to determine  $(v_x, v_y, h, \rho, \mathbf{R}_S^*)(t)$  from  $O(\mathbf{R}_S, \mathbf{R}_T, \mathbf{L}) \triangleq (\mathbf{R}_S, \mathbf{R}_T, FS(\mathbf{L}))$ , where the operator  $O$  maps from the current system configuration to its observation.

#### IV. PARAMETER LEARNING

In this section, we present our preprocessing algorithm that uses supervised learning to predict the dynamic characteristics of a liquid body. As part of the feedback planner, the learning algorithm is used to infer the parameters  $(v_x, v_y, h, \rho, \mathbf{R}_S^*)(t)$  from the observations  $O(\mathbf{R}_S, \mathbf{R}_T, \mathbf{L})(t)$ . We use a neural network that is trained from a set of successful transfer trajectories. These underlying parameters are used to infer the following properties: The first four parameters  $(v_x, v_y, h, \rho)$  specify the liquid outflow position, so that to infer these four parameters is a system identification problem. On the other hand, the last parameter  $\mathbf{R}_S^*$  specifies the action we should take for that observation. As a result, inferring the last parameter is a policy search problem. According to Equation 2, the final action is computed by following  $\mathbf{R}_S^*$  as much as possible and performing local adjustments based on the values of  $(v_x, v_y, h, \rho)$ . In theory, it is possible to simplify our online feedback motion planning algorithm and have the neural network output directly the final action. However, according to our experiments, using an exact spacetime optimization will result in much better results.

Our mapping function from  $O(\mathbf{R}_S, \mathbf{R}_T, \mathbf{L})(t)$  to  $(v_x, v_y, h, \rho, \mathbf{R}_S^*)(t)$  is defined using a neural network illustrated in Figure 4. We take previous observations  $FS(P_L)(t-1)$  and  $FS(P_L)(t-2)$  as additional inputs because the liquid velocity may not be available in our observations, and the additional inputs help the network to recover this velocity information from shape differentiation. Our network has four fully connected layers  $(H_1, H_2, H_3, H_4)$ . The first two layers  $(H_1, H_2)$  of our network are used to predict the liquid outflow position and we use a separate loss function. The predicted quadratic curve is concatenated with the rigid body observation and fed to the last two layers  $(H_3, H_4)$  to predict the mean trajectory prior.

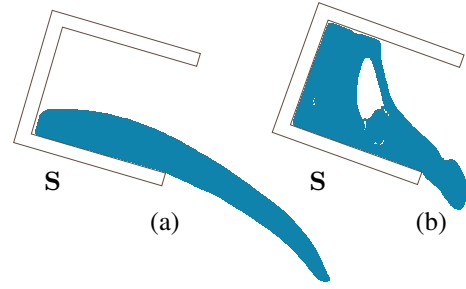


**Fig. 5:** There are many ways we can successfully transfer the liquid. For example, we usually turn  $\mathbf{S}$  slowly so that the liquid follows a laminar flow out of  $\mathbf{S}$  (a). Or we can turn  $\mathbf{S}$  quickly so that the breaking wave on free-surface pushes the liquid violently out of  $\mathbf{S}$  (b).

A missing component of this model is that we do not predict future liquid height fields  $FS(P_L)(t+1)$  from current  $FS(P_L)(t)$ , which is required to solve Equation 2. In our current method, we just set  $FS(P_L)(t+1) = FS(P_L)(t)$ .

#### A. TRAINING DATA GENERATION

Our training dataset includes a large set of groundtruth observations  $O$ , the liquid outflow position, and the mean trajectory prior. As noted by [29], [30], this training dataset must be generated carefully so that it can be represented by the neural network. For example, it is well known that liquid flow can be categorized into laminar flow and turbulent flow. It is very unlikely that the small network in Figure 4 can represent both of the transfer trajectories that induce laminar flow (Figure 5 (a)) and turbulent flow (Figure 5 (b)), although they are both successful transfers. Indeed, even the definition of liquid height field  $FS(P_L)$  in Figure 5 (b) is ambiguous due to the air bubble in the liquid body. Therefore, the training dataset must be focused on liquid transfer using only laminar flow.

Both [29] and [30] address this problem for some applications by modifying the dataset during training. [29] assumes there is an expert who can provide additional training samples on request for error recovery. However, our approach does not assume the presence of any such expert. A human demonstrator may serve as a good expert, but digitizing or capturing the liquid shape trajectory can be very challenging. On the other hand, [30] assumes that the governing equation Equation 1 is differentiable with respect to  $u$ . This assumption does not hold due to the non-smooth free-surface changes. Moreover, the computational complexity of [30] makes it infeasible for the high-dimensional configuration space of a liquid body.

In order to handle these issues, we use a stochastic optimization algorithm to automatically compute useful training dataset [3]. To ensure that the training dataset is useful and representable, we design a problem specific search space so that the optimized trajectories always lead to laminar flow. Given an instance of the problem:  $\mathbf{P}(\mathbf{D}_{ST}, \mathbf{V}_T, f)$ , our optimizer computes a groundtruth plan  $\mathcal{P}$  that maximizes a reward function  $R$ . We use the following definition for  $R$  to

measure the quality of  $\mathcal{P}$ :

$$\begin{aligned} \Delta_{i,j} &\triangleq P_L^j(t_i) - \mathbf{R}_T(t_i)\mathbf{O}_T \\ R &= \sum_i \sum_j \mathcal{I}[\Delta_{i,j}^y \Delta_{i-1,j}^y < 0] (R_{i,j}^1 + R_{i,j}^2) \\ R_{i,j}^1 &\triangleq \frac{\Delta\mathbf{O} - \text{abs}(\Delta_{i,j}^x)}{\Delta\mathbf{O}} \\ R_{i,j}^2 &\triangleq -100\mathcal{I}[\Delta\mathbf{O} - \text{abs}(\Delta_{i,j}^x) < 0], \end{aligned} \quad (3)$$

where the first term of  $R$  indicates that particle  $P_L^j$  passes through the opening of  $\mathbf{T}$  at timestep  $i$ . If this is the case, we assign a positive reward if the particle falls inside  $\mathbf{T}$  and a negative reward, otherwise. The reward is higher when the particle is closer to the center  $\mathbf{O}_T$ .

Even though we have all the components to formulate the stochastic optimization problem, the dimension of the resulting search space  $\mathcal{P}$  is too high. The parameters  $(x_S, y_S, \alpha)(t_i)$  for each  $t_i$  need to be determined. In order to compute the local minima in this space, we need a large number of samples in  $\mathcal{P}$ . This can significantly slow down the optimization as evaluating  $R$  for each sample would involve a fluid resimulation, which can take several minutes, even for a 2D workspace. Another closely related issue is that searching directly in  $\mathcal{P}$  can result in training samples that cannot be represented by the neural network, because there are no guarantees that only laminar flows (e.g. Figure 5 (a)) are generated. Therefore, we have to use a more restrictive search space. First, we only search for  $(x_S, y_S, \alpha)(t_i)$  at 6 key time instances:  $(t_0, t_{N/5}, t_{2N/5}, t_{3N/5}, t_{4N/5}, t_N)$  and use linear interpolation for other timesteps. We further assume the following constraints:

$$\begin{aligned} \Delta_i &\triangleq \mathbf{R}_S(s_i)\mathbf{O}_S - \mathbf{R}_T(t_i)\mathbf{O}_T \\ \text{abs}(\Delta_i^x) &< \text{abs}(\Delta_{i-1}^x) \quad \text{abs}(\Delta_i^y) < \text{abs}(\Delta_{i-1}^y) \\ \alpha(t_i) &> \alpha(t_{i-1}). \end{aligned}$$

Intuitively, these conditions require that  $\mathbf{S}$  is always approaching  $\mathbf{T}$  and increasing its turning angle. We enforce these constraints by transforming the search space to the unit box domain:

$$\left( \frac{\text{abs}(\Delta_{iN/5}^x)}{\text{abs}(\Delta_{(i-1)N/5}^x)}, \frac{\text{abs}(\Delta_{iN/5}^y)}{\text{abs}(\Delta_{(i-1)N/5}^y)}, \frac{\alpha_{max} - \alpha(t_{iN/5})}{\alpha_{max} - \alpha(t_{(i-1)N/5})} \right) \in (0, 1]^3, \quad (4)$$

and using CMA-ES [31] to perform the stochastic search, where  $\alpha_{max}$  is our max allowable turning angle. Finally, we modify CMA-ES to only accept solutions that are collision-free, so that the computed mean trajectory prior has the same collision-free property.

In our experiments, all the resulting trajectories exhibit laminar liquid flow. From these trajectories, we extract groundtruth observation  $O(\mathbf{R}_S, \mathbf{R}_T, \mathbf{L})(t) = (\mathbf{R}_S, \mathbf{R}_T, FS(P_L))(t_i)$  and label  $(v_x, v_y, h, \rho, \mathbf{R}_S^*)(t_i)$  for each timestep  $t_i$ . To extract the quadratic curve parameters, we use the same greedy quadratic curve fitting method as [4]. In the second stage, we train the neural network illustrated in Figure 4, where we use 32 hidden neurons for each of the four hidden layers. Note that the ReLU activation function is used for each hidden layer except for the output layer, where we used Sigmoid activation

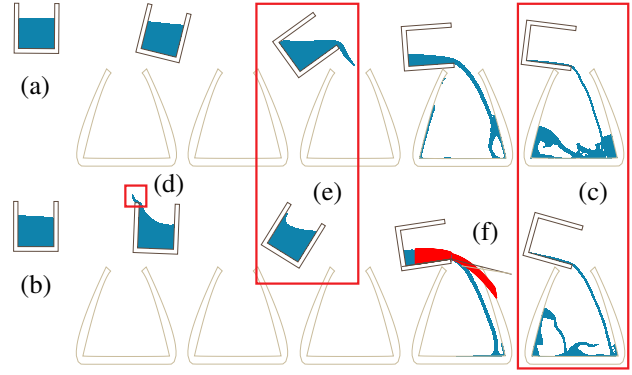


**Fig. 6:** We illustrate an exemplary trajectory of TRANSFER (a) and TRANSFER+SPILL (b). On convergence of CMA-ES optimization, the liquid flow is well centered around  $\mathbf{O}_T$  (c). TRANSFER+SPILL encourages spilling at an early stage of pouring (d), so that  $\mathbf{S}$  must move and turn slowly (e). For each timestep in each trajectory, we extract the ground truth water height field and liquid outflow position as training dataset (f).

function. This is because we applied the same trick of domain transformation. Instead of outputting  $(x_S, y_S, \alpha)$ , our network outputs  $\left( \frac{\text{abs}(\Delta_{t_i}^x)}{\text{abs}(\Delta_{t_{i-1}}^x)}, \frac{\text{abs}(\Delta_{t_i}^y)}{\text{abs}(\Delta_{t_{i-1}}^y)}, \frac{\alpha_{max} - \alpha(t_i)}{\alpha_{max} - \alpha(t_{i-1})} \right)$  which belongs exactly to the range of Sigmoid function. Our final stage is the online control stage, where for each timestep  $t_i$ , we query the neural network for parameters, then plug them into Equation 2 and solve for our final action  $\dot{\mathbf{R}}_S(t_i)$ .

## V. RESULTS

**Analysis:** We evaluate the online and offline phase in Figure 1 using a series of experiments. First, we need to evaluate the effectiveness of our dataset. All the trajectories in our dataset reside in a 2D workspace. The cost of generating these trajectories is:  $\mathcal{O}(\#iteration \times \#problem \times \#timestep \times |\{P_L\}|)$ , where  $\#iteration$  is the number of fluid resimulations needed in each CMA-ES optimization,  $\#problem$  is the number of problems  $\mathbf{P}$  to generate, and finally  $\#frame$  is the number of timesteps in each fluid simulation. In a 2D workspace, the last term  $|\{P_L\}|$  is less than  $10^5$ ; while  $|\{P_L\}|$  in a 3D workspace can easily reach a million. Therefore, generating a 3D dataset is orders of magnitude more expensive. Second, we need to verify that our neural network structure can accurately predict the liquid outflow position as well as the mean trajectory prior. Finally, we will analyze the performance of the online feedback planner.

**Dataset:** We generated two datasets named TRANSFER and TRANSFER+SPILL using parameters listed in I. Since each function evaluation amounts to a fluid resimulation, the generation of TRANSFER and TRANSFER+SPILL involves  $6 \times 10^6$  fluid simulations. We run CMA-ES in a 2D workspace and the computation takes 2 weeks on a 1000 core cluster. TRANSFER and TRANSFER+SPILL differ in the initial liquid configuration. In TRANSFER, the initial liquid velocity follows that of  $\mathbf{S}$ , which is typical if the liquid has moved with  $\mathbf{S}$  for a distance and reached equilibrium. However, in

Parameter	Value (Unit)
Number of problem: $\#P$	1000
The range of $D_{ST}: L$	3m
The range of $V_T: V$	5(m/s)
The range of fill level: $[f_{min}, f_{max}]$	$[0.3, 0.8]$
CMA-ES population size	30
CMA-ES iterations	200
$\alpha_{max}$	$120^\circ$

**TABLE I:** The parameters used to generate random problem  $P$ , setup CMA-ES, and generate TRANSFER and TRANSFER+SPILL dataset.

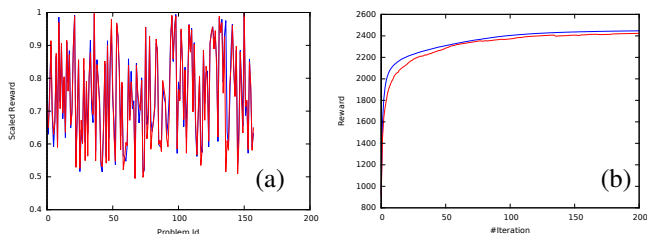


**Fig. 7:** (a): The scaled reward function  $R/\#P_L$  across a set of transfer problems in TRANSFER (blue) and TRANSFER+SPILL (red). These values are all positive, meaning that very little spilling happens and particles are well centered around  $O_T$ . (b): The average convergence history of CMA-ES algorithm.

TRANSFER+SPILL, the initial liquid velocity is zero, which is typical if we start transfer from a stationary scenario. Problems in TRANSFER+SPILL are considered harder than those in TRANSFER, as moving  $S$  too quickly will lead to spilling and thus negative reward. These two datasets can be downloaded at <http://gamma.cs.unc.edu/FluidMotion> and are illustrated in Figure 6. Figure 7 shows the distribution of scaled reward function  $R/\#P_L$  in TRANSFER and TRANSFER+SPILL as well as the CMA-ES convergence history. This figure verifies that the dataset does contain successful transfer trajectories. Further we need to verify that the generated trajectories always transfer liquid using laminar flow, instead of turbulent flow. We note that the velocity field of a laminar flow should have no internal vortex. Therefore, we compute the vortical velocity component and plot its strength relative to the original velocity field in Figure 8. This figure shows clearly that the trajectories in both TRANSFER and TRANSFER+SPILL use only laminar flow.

**Neural Network:** Our neural network serves two purposes for which we conduct separate experiments. Our first step is to verify the accuracy of the liquid outflow position predictor by testing it on 100 randomly selected trajectories in TRANSFER/TRANSFER+SPILL, i.e. testing using the training dataset. Then we test it on 100 new trajectories  $\mathcal{P}$  randomly generated by spline interpolation. Figure 9 (a) plots the averaged accuracy against the turning angle  $\alpha$ . This plot reveals that our predictor has low accuracy at a small turning angle. These erroneous configurations are illustrated in Figure 9 (b). The reason for the low accuracy is that liquid is subject to the surface tension force around the lip of source container opening  $O_S$ , and our fluid

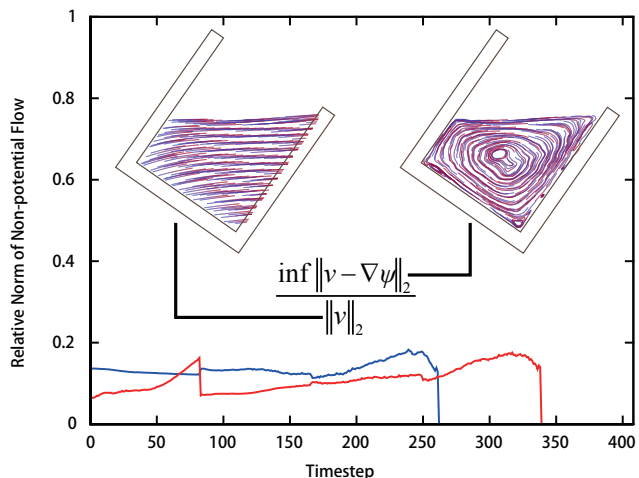


**Fig. 8:** We picked 100 random trajectories in TRANSFER (blue) and TRANSFER+SPILL (red) dataset, and visualized the temporal change of the relative strength of vortical velocity component. Since this value is always less than 0.2, the flow is very close to a potential flow. Since problems in the TRANSFER dataset are easier, the pouring is usually completed faster, which is consistent with the early termination of blue curve.

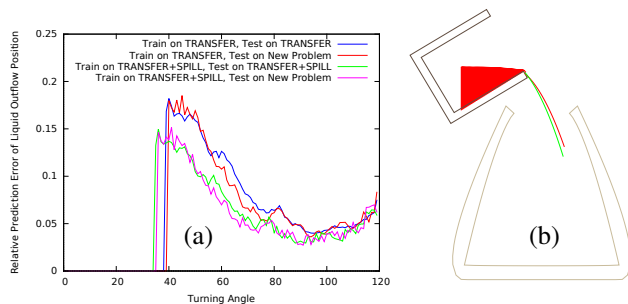


**Fig. 9:** (a): The relative error of neural network’s liquid outflow position predictor plotted against the turning angle  $\alpha$ . (b): A typical failure case where the predicted quadratic curve (green) deviates from the groundtruth curve (red). This usually happens when the liquid body is subject to surface tension forces around  $O_S$ .

simulator is not accurate enough to model this phenomenon. Usually, modelling surface tension requires a higher particle resolution around  $O_S$ . However, surface tension will just pull liquid closer to  $S$  and this general trend is still captured by our model.

We further validate the accuracy of the mean trajectory prior predictor. Figure 10 (a) illustrates the relative accuracy of  $\hat{R}_S^*$  compared with ground truth. The error is higher than that of the liquid outflow position predictor. It is the responsibility of our online feedback motion planner to compensate for this error. In addition, we conduct another experiment to see if our predictor has the ability to avoid spilling. Since we know that TRANSFER does not model spilling but TRANSFER+SPILL does, we plot in Figure 10 (b) the predicted temporal change of  $\alpha$  using TRANSFER and TRANSFER+SPILL as training dataset. Our predictor trained using the TRANSFER+SPILL dataset prefers a lower  $\dot{\alpha}$  at small  $\alpha$ , meaning that our network does learn to avoid spilling.

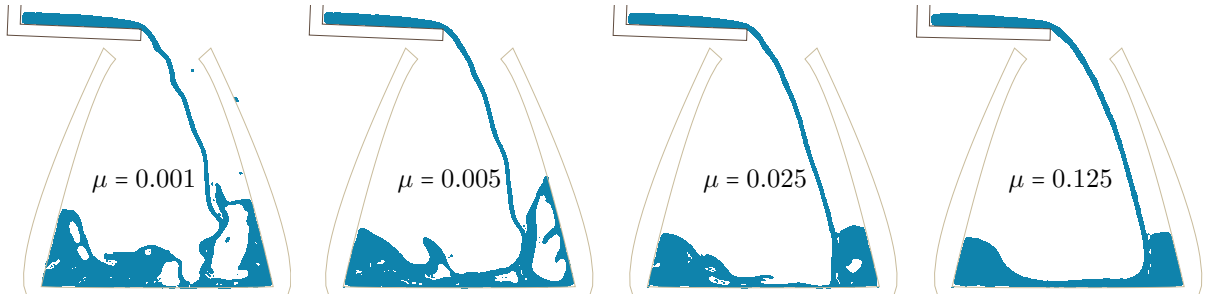


**Fig. 11:** We tested our feedback controller on new fluid materials with higher dynamic viscosity ( $kg/(ms)$ ). In this case, we achieved even higher online reward.

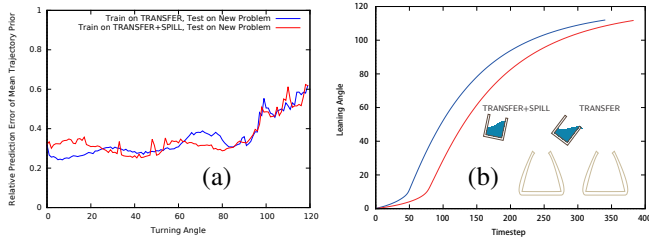


**Fig. 10:** (a): The relative error of predicted  $\hat{\mathbf{R}}_S^*$  plotted against turning angle. (b): The predicted  $\alpha$  plotted against timestep index: the mean trajectory prior predictor trained using TRANSFER+SPILL dataset (red) does learn to turn  $\mathbf{S}$  slowly to avoid spilling, compared with the predictor trained using TRANSFER dataset (blue). We also show such difference using one exemplary frame of a testing problem.

**Feedback Controller:** In the online phase, we solve Equation 2 using a horizon length of  $K = 25$ . This requires querying the neural network 25 times and performing an optimization, for which we use a LBFGS optimizer. Due to the small size of our neural network and the optimization problem, this process can be accomplished at more than 200fps on a desktop machine. We tested our feedback controller using 20 new testing problems. The online positive reward per particle is plotted in Figure 12 (a) for each problem. We can see that the liquid is very well centered around  $\mathbf{O}_T$ . In Figure 12 (b), we plotted the fraction of liquid particles that goes outside  $\mathbf{T}$ . Both planners can keep a very low level of spilling in most cases, the planner trained using TRANSFER+SPILL dataset performs especially well since it is trained to avoid spilling. Finally, we show the versatility of our controller by testing it on problems not seen in TRANSFER and TRANSFER+SPILL. In Figure 11, we test on fluid with a higher dynamic viscosity coefficient than that in the training dataset. In this case, the achieved online reward is even higher than Figure 12 (a). This is consistent with the fact that higher viscosity will encourage laminar flow. In Figure 13 (a), we introduce an additional dynamic obstacle which is handled by  $C_o$  in Equation 2. Finally, we can test our controller on a 3D workspace, by applying the controller only to the 2D cross-section of  $\mathbf{S}$  and  $\mathbf{T}$ , as illustrated in Figure 13 (b).

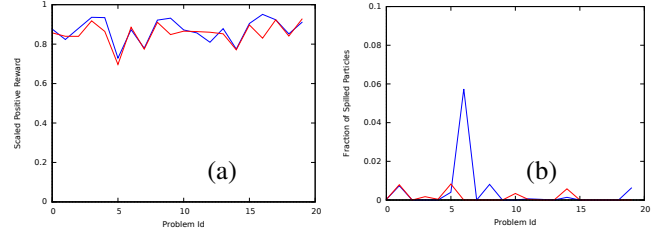


**Fig. 12:** (a): The average positive reward per particle  $\mathbf{P}_L$  in 20 testing problems, with neural network trained using TRANSFER dataset (blue) and TRANSFER+SPILL dataset (red). Both planners can center liquid particles around  $\mathbf{O}_T$  but the planner using TRANSFER dataset usually gives slightly higher reward. (b): The fraction of spilled liquid particles (TRANSFER dataset in blue and TRANSFER+SPILL dataset in red). In all problems except for the 6th, we observe almost no spilling using both planners.

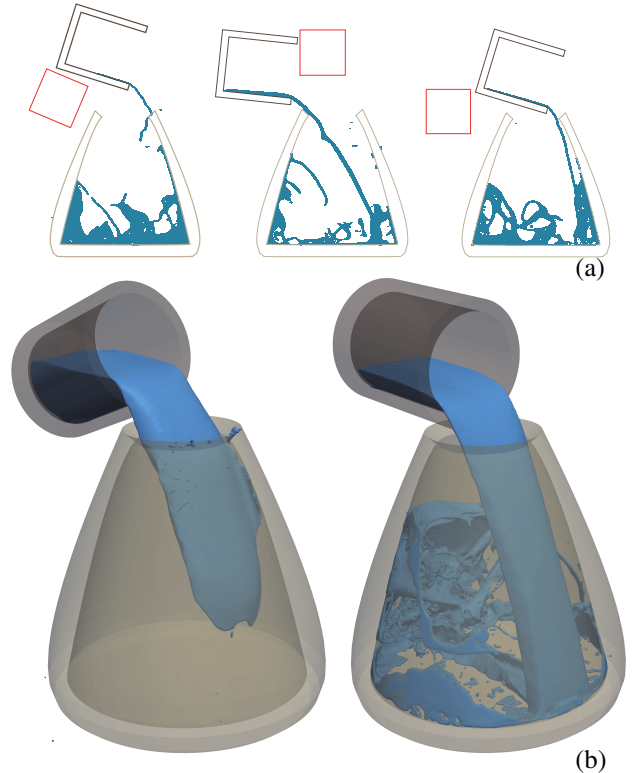


**Fig. 13:** (a): Examples with dynamic obstacles. (b): A frame of our controller applied to a 3D workspace. The controller only sees the 2D cross section.

## VI. LIMITATIONS AND CONCLUSIONS

In this work, we propose a feedback motion planner for liquid transfer problems. The method is an optimization-based receding horizon planner, which is guided by a machine learning model that provides clues for global movement (mean trajectory prior) and local adjustment (liquid outflow position). Our experiments show that the planning framework can achieve promising online performance and the machine learning model gains important skills in pouring such as spilling avoidance and liquid position prediction.

A major limitation of our method is that the dataset generation is computationally very costly even in a 2D workspace. Although our system is 3D capable, generating a 3D dataset is still impractical even with a cluster at hand. A practical compromise is to train on a 2D dataset and test on 3D problems as is done in Figure 13 (b). Simply considering the cross section is not enough, however, since liquid can fall outside  $\mathbf{T}$  from other directions and this is not modelled by our method. Also, we do not model the behavior of the liquid body after it falls into  $\mathbf{T}$ . This choice allows us to handle different fluid materials (in terms of viscosity) because they only exhibit different behaviors, such as coiling and buckling, after falling into  $\mathbf{T}$ . On the downside, liquid particles can jump out of  $\mathbf{T}$  again after falling into it, and this kind of spilling is also ignored by not modelling liquid body in  $\mathbf{T}$ . Finally, we have not tested this system on a real robot, which requires additional kinematic and dynamic constraints.

## REFERENCES

- [1] M. Kalakrishnan, S. Chitta, E. Theodorou, P. Pastor, and S. Schaal, "STOMP: Stochastic trajectory optimization for motion planning," in *Proceedings of IEEE International Conference on Robotics and Automation*, 2011, pp. 4569–4574.
- [2] J. Schulman, Y. Duan, J. Ho, A. Lee, I. Awwal, H. Bradlow, J. Pan, S. Patil, K. Goldberg, and P. Abbeel, "Motion planning with sequential convex optimization and convex collision checking," *The International Journal of Robotics Research*, vol. 33, no. 9, pp. 1251–1270, 2014.
- [3] Y. Kuriyama, K. Yano, and M. Hamaguchi, "Trajectory planning for meal assist robot considering spilling avoidance," in *Control Applications, 2008. CCA 2008. IEEE International Conference on*. IEEE, 2008, pp. 1220–1225.
- [4] Z. Pan, C. Park, and D. Manocha, "Robot motion planning for pouring liquids," in *Proceedings of International Conference on Automated Planning and Scheduling*, 2016.
- [5] L. Kunze, M. E. Dolha, E. Guzman, and M. Beetz, "Simulation-based temporal projection of everyday robot object manipulation," in *The 10th International Conference on Autonomous Agents and Multiagent Systems-Volume 1*. International Foundation for Autonomous Agents and Multiagent Systems, 2011, pp. 107–114.
- [6] M. Tzamtzi and F. Koumboulis, "Robustness of a robot control scheme for liquid transfer," in *Novel Algorithms and Techniques In Telecommunications, Automation and Industrial Electronics*. Springer, 2008, pp. 156–161.
- [7] Z. Pan and D. Manocha, "Motion planning for fluid manipulation using simplified dynamics," in *IEEE/RSJ International Conference on Intelligent Robots and Systems*. IEEE, 2016.
- [8] S. M. Lavalley, "Rapidly-exploring random trees: A new tool for path planning," 1998.
- [9] D. Wilkie, J. P. van den Berg, and D. Manocha, "Generalized velocity obstacles," in *Proceedings of IEEE/RSJ International Conference on Intelligent Robots and Systems*, 2009, pp. 5573–5578.
- [10] M. Stilman, "Task constrained motion planning in robot joint space," in *IEEE/RSJ International Conference on Intelligent Robots and Systems*, 2007, pp. 3074–3081.
- [11] D. Berenson, S. S. Srinivasa, D. Ferguson, A. Collet, and J. J. Kuffner, "Manipulation planning with workspace goal regions," in *Proceedings of IEEE International Conference on Robotics and Automation*, 2009, pp. 618–624.
- [12] C. Park, J. Pan, and D. Manocha, "ITOMP: Incremental trajectory optimization for real-time replanning in dynamic environments," in *Proceedings of International Conference on Automated Planning and Scheduling*, 2012.
- [13] D. Ferguson, N. Kalra, and A. Stentz, "Replanning with rrts," in *Proceedings 2006 IEEE International Conference on Robotics and Automation, 2006. ICRA 2006*. IEEE, 2006, pp. 1243–1248.
- [14] K. Hauser, "On responsiveness, safety, and completeness in real-time motion planning," *Autonomous Robots*, vol. 32, no. 1, pp. 35–48, 2012.
- [15] S. Koenig and M. Likhachev, "Fast replanning for navigation in unknown terrain," *IEEE Transactions on Robotics*, vol. 21, no. 3, pp. 354–363, 2005.
- [16] M. Daswani, P. Sunehag, M. Hutter, et al., "Feature reinforcement learning: state of the art," in *Sequential decision-making with big data: papers from the AAAI-14 workshop*. Association for the Advancement of Artificial Intelligence, 2014.
- [17] H. Kurniawati, D. Hsu, and W. S. Lee, "Sarsop: Efficient point-based pomdp planning by approximating optimally reachable belief spaces," in *In Proc. Robotics: Science and Systems*, 2008.
- [18] S. Levine and P. Abbeel, "Learning neural network policies with guided policy search under unknown dynamics," in *Advances in Neural Information Processing Systems*, 2014, pp. 1071–1079.
- [19] C. Park, J. Pan, and D. Manocha, "High-dof robots in dynamic environments using incremental trajectory optimization," *International Journal of Humanoid Robotics*, vol. 11, no. 02, p. 1441001, 2014.
- [20] J. Schulman, J. Ho, C. Lee, and P. Abbeel, "Learning from demonstrations through the use of non-rigid registration," in *Robotics Research*. Springer, 2016, pp. 339–354.
- [21] Y. Li, Y. Yue, D. Xu, E. Grinspun, and P. K. Allen, "Folding deformable objects using predictive simulation and trajectory optimization," in *Intelligent Robots and Systems (IROS), 2015 IEEE/RSJ International Conference on*. IEEE, 2015, pp. 6000–6006.
- [22] N. Chentanez, R. Alterovitz, D. Ritchie, L. Cho, K. K. Hauser, K. Goldberg, J. R. Shewchuk, and J. F. O'Brien, "Interactive simulation of surgical needle insertion and steering," in *Proceedings of ACM SIGGRAPH 2009*, Aug 2009, pp. 88:1–10. [Online]. Available: <http://graphics.berkeley.edu/papers/Chentanez-ISBN-2009-08/>
- [23] A. Treuille, A. McNamara, Z. Popović, and J. Stam, "Keyframe control of smoke simulations," in *ACM Transactions on Graphics (TOG)*, vol. 22, no. 3. ACM, 2003, pp. 716–723.
- [24] Z. Pan and D. Manocha, "Motion planning for fluid manipulation using simplified dynamics," *CoRR*, vol. abs/1603.02347, 2016. [Online]. Available: <http://arxiv.org/abs/1603.02347>
- [25] X. B. Peng, G. Berseth, and M. van de Panne, "Terrain-adaptive locomotion skills using deep reinforcement learning," *ACM Transactions on Graphics (Proc. SIGGRAPH 2016)*, vol. 35, no. 5, 2016, to appear.
- [26] C. Bowen and R. Alterovitz, "Closed-loop global motion planning for reactive execution of learned tasks," in *2014 IEEE/RSJ International Conference on Intelligent Robots and Systems*. IEEE, 2014, pp. 1754–1760.
- [27] H. Wang, M. Liao, Q. Zhang, R. Yang, and G. Turk, "Physically guided liquid surface modeling from videos," in *ACM Transactions on Graphics (TOG)*, vol. 28, no. 3. ACM, 2009, p. 90.
- [28] J. Gregson, M. Krimerman, M. B. Hullin, and W. Heidrich, "Stochastic tomography and its applications in 3d imaging of mixing fluids," *ACM Trans. Graph.*, vol. 31, no. 4, pp. 52–1, 2012.
- [29] S. Ross, G. J. Gordon, and D. Bagnell, "A reduction of imitation learning and structured prediction to no-regret online learning," in *Proceedings of the Fourteenth International Conference on Artificial Intelligence and Statistics (AISTATS-11)*, G. J. Gordon and D. B. Dunson, Eds., vol. 15. Journal of Machine Learning Research - Workshop and Conference Proceedings, 2011, pp. 627–635. [Online]. Available: <http://www.jmlr.org/proceedings/papers/v15/ross11a/ross11a.pdf>
- [30] S. Levine and V. Koltun, "Learning complex neural network policies with trajectory optimization," in *ICML '14: Proceedings of the 31st International Conference on Machine Learning*, 2014.
- [31] N. Hansen, "The cma evolution strategy: A tutorial," *arXiv preprint arXiv:1604.00772*, 2016.
- [32] S. Karaman and E. Frazzoli, "Sampling-based algorithms for optimal

motion planning,” *The International Journal of Robotics Research*, vol. 30, no. 7, pp. 846–894, 2011.

- [33] A. Punjani and P. Abbeel, “Deep learning helicopter dynamics models,” in *2015 IEEE International Conference on Robotics and Automation (ICRA)*. IEEE, 2015, pp. 3223–3230.